

# Soft Matter

Accepted Manuscript



This is an *Accepted Manuscript*, which has been through the Royal Society of Chemistry peer review process and has been accepted for publication.

*Accepted Manuscripts* are published online shortly after acceptance, before technical editing, formatting and proof reading. Using this free service, authors can make their results available to the community, in citable form, before we publish the edited article. We will replace this *Accepted Manuscript* with the edited and formatted *Advance Article* as soon as it is available.

You can find more information about *Accepted Manuscripts* in the [Information for Authors](#).

Please note that technical editing may introduce minor changes to the text and/or graphics, which may alter content. The journal's standard [Terms & Conditions](#) and the [Ethical guidelines](#) still apply. In no event shall the Royal Society of Chemistry be held responsible for any errors or omissions in this *Accepted Manuscript* or any consequences arising from the use of any information it contains.

Cite this: DOI: 10.1039/c0xx00000x

www.rsc.org/xxxxxx

**ARTICLE TYPE**

# Mesoscopic Simulation of the Self-assembly of the Weak Polyelectrolyte Poly(ethylene oxide)-*block*-Poly(methyl methacrylate) Diblock Copolymers

Dan Mu<sup>\*a</sup>, Jian-Quan Li<sup>\*b</sup> and Sheng-Yu Feng<sup>\*c</sup>

5 Received (in XXX, XXX) Xth XXXXXXXXX 20XX, Accepted Xth XXXXXXXXX 20XX  
DOI: 10.1039/b000000x

We designed twelve types of weak polyelectrolytes (i.e., PEO-*b*-PMMA copolymers (BCP) in multi-arm structures, where six include EO block as joint points and the other six have MMA block as joint points). All of the BCPs with A as the joint points form disordered phases with the exception of long-chained and  
10 four-armed BCP. The main mesophases of all of the BCPs with B as joint points are micelle-like, bicontinuous phases. In particular, the short-chained BCP with four-arms and EO segments outside form a new phase type (i.e., crossed lamellar phase). Using MesoDyn, we provide a comprehensive representation of the micelle and crossed lamellar phase formation mechanisms based on both  
15 thermodynamic and dynamic analyses. A shear force on a micelle-like phase could promote a hexagonal columnar phase, which is a good technique for generating an ordered arrangement of nanotube arrays. Blending homopolymers with the same constituents could promote uniformity of the micelle size and decrease the polydispersity, especially for blends with a high BCP concentration, which may provide a new approach for regulating the properties of materials.

## 1 Introduction

20 The molecular self-assembly [1-2] has attracted a great deal of interest because of its fundamental importance in understanding cellular evolution and its applications in mimicking biological functions and constructing smart nanomaterials. Compared with small molecular aggregates, polymer aggregates exhibit higher  
25 stability and durability, owing to their mechanical and physical properties. Therefore, polymer self-assembly has many potential applications in biomedicine, biomaterials, microelectronics, photoelectric materials, catalysts, etc [3-6]. The phase separation mechanisms by thermal induction have been classified into: (i) nucleation and growth, where droplets of the minority phase coarsen if they exceed a threshold size; (ii) spinodal decomposition, where the mixed phase becomes unstable and separates into co-continuous arrangement of domains [7]. Tanaka et. Al found a new and unusual phase separation in dynamically  
30 asymmetric mixtures, called viscoelastic phase separation [8-10]. The polyelectrolytes are polymers with ionizable groups on constituent monomers. Polyelectrolytes are ubiquitous in nature and in applications ranging from personal care products to paints, coatings and processed foods. Indeed, all biopolymers are  
35 polyelectrolytes. The existence of both short-range (excluded volume) and long-range (electrostatic) interactions leads to the behavior of the polyelectrolytes being different from neutral polymers [11-14]. Some experiments have shown that a large number of flexible polyelectrolytes can form different aggregates  
40 (e.g., spherical [15] or cylindrical micelles [16-17]) in a three-

dimensional network via covalent crosslinks. In addition, extensive theoretical and computational investigations of polyelectrolytes have been performed over the past few decades[18-26].

50 The poly(ethylene oxide) (PEO) segment contains a hydroxyl group in the last monomer of its tail, which is cationic, but the monomer consists of one oxygen atom in an ester group and hydrocarbon groups, which is anionic. For the poly(methyl methacrylate) (PMMA) segment, a carbonyl group also exists in  
55 the tail and the electrostatics contributions from the cationic (0.017 e) and anionic (-0.0085 e) parts, as the result from the quantum calculations shown, they are so weak that can be neglected. Therefore, both the PEO and PMMA segments, which arrange in a certain topology to form a block copolymer, are  
60 weak polyelectrolyte molecules. The semicrystalline nature of PEO and the similar solubility parameters of both PEO and PMMA make it an attractive system.

Computer simulation methods are valuable tools for investigating the behaviors of polymers on the micro- to macroscale. Molecular  
65 simulation is not suitable for the calculations on the phase behavior of polymer systems due to the extremely large computational load. However, mesoscopic dynamic simulation acts as a bridge between fast molecular kinetics and slow thermodynamic relaxation of macroscale properties. MesoDyn  
70 density functional theory is suitable for exploring the self-assembly behavior of polymers on the mesoscale level. This method was developed by Fraaije [27-28], which can be employed to investigate the phase separation dynamics and ordering processes of the polymeric systems via the description

by Langevin equations.

In our previous study [29], the Flory-Huggins parameters,  $\chi$ , were calculated in a wide range of blending ratio composites of PEO and PMMA at the atomic level. The calculated lower critical solution temperature (LCST) behavior at high temperature, i.e., 400 K, was in agreement with the experimental result and clarified the conflicting conclusions drawn from different techniques and laboratories. This result is a good starting point for the bottom-up design of purpose-specific materials from the atomistic level. An additional investigation at the mesoscopic level is performed in this study, and this study is grounded in the fundamental molecular behavior rather than empirical results to provide, a comprehensive understanding of the structure-property

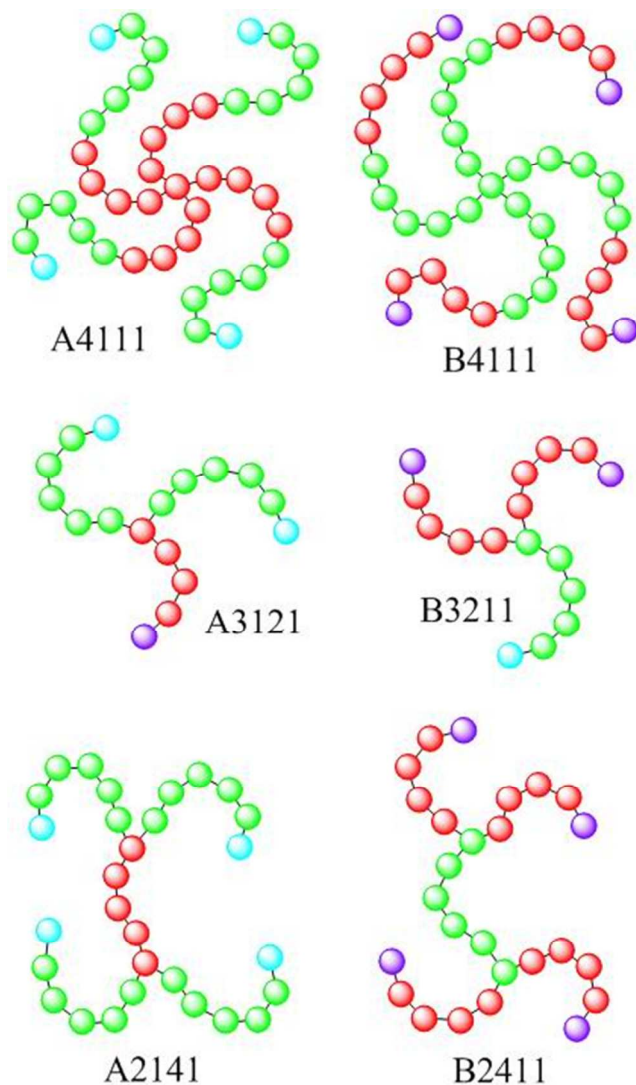


**Fig. 1** Schematic representation of PEO-*b*-PMMA BCPs with short chains. The red particles represent the EO blocks denoted as A, and A' is the terminal of the A segments, which are shown in purple. The green particles in the MMA blocks are denoted as B, and B' is the terminal of the B segments, which are shown in cyan.

relationships from nano- to mesoscale. The primary goal of this study was to determine whether the lipid-structured polyelectrolytes behave in a similar fashion to lipid molecules via mesoscopic modeling. An additional motive was to gain insight

into the mechanism. Such a finer-to-coarse, hierarchical framework can facilitate nanoscale material design from the molecular to mesoscale level.

## 2 Models and Parameter Settings

The models in MesoDyn are coarse-grained into Gaussian chains where all of the segments are the same size, and the chain topology depends on the degree of coarsening of the original chains. The Gaussian chain density functions consist of a one-to-one relationship between the external potential fields and the density fields for each bead type. The chemical potentials are the functions of the external potentials and the density fields. The coupled Langevin equations represent the relationship between the time derivatives and the chemical potentials. The noise is related to the exchange kinetic coefficients.

At first, the solubility parameters of various chain lengths of both PEO and PMMA homopolymers were calculated by Molecular Dynamic methods, then we found the solubility parameters would be stable at a certain value with the increase in the chain length. With the comparison of the experimental values of their solubility parameters, the representative chain lengths of 50 for both PEO and PMMA chain can be decided as the representative bulk chain lengths in this simulation. Divided by the characteristic ratio, two Gaussian chains of A<sub>5</sub> and B<sub>6</sub> (A denotes EO bead and B denotes MMA bead) were generated to represent the atomistic chains of polymer PEO<sub>50</sub> and PMMA<sub>50</sub> [29]. We set A<sub>5</sub>B<sub>6</sub> as a basic unit in the investigated PEO-*b*-PMMA block copolymers (BCP). In an attempt to mimic the lipid-like structures, a strategy consisting of miktoarm with A<sub>5</sub> and B<sub>6</sub> as basic segments was introduced. The six types of chain topologies in this process shown in Fig. 1. To distinguish the different electrostatic interactions between various segments, we set "A" to be the repeat monomers of PEO, "A'" to denote the terminal with the hydroxyl group, and "B" to represent the repeat monomers of PMMA, and "B'" is the terminal part. The naming scheme of these BCPs is as follows: the letter denotes the bead type of the branched point, the first number shows the arm number for each branched point, the following two numbers represent the ratio of the A to B segment, and the last number indicates the chain length via the multiple of the A<sub>5</sub> and B<sub>6</sub> segment. A single enlarging of the segment lengths of the six BCPs is helpful for investigating the phase morphologies of different chain lengths. For example, the name B2412 indicates this BCP consists of two branched points constructed by a B bead, each branched point has two arms, the ratio of A and B segment is 4:1, and each of the A and B segments has a chain length that is twice as long as that of the A<sub>5</sub> and B<sub>6</sub> segments. The molecular information for the twelve BCPs is listed in Table 1.

**Table 1** Molecular information for the BCPs.

Name	Arm number in each branch point	Ratio of A to B segments	Chain length*	Molecular structure
A4111	4	1:1	1	$A(A_4B_5B')_4$
A3121	3	1:2	1	$A'A_4(B_5B')_2$
A2141	2	1:4	1	$(B'B_5)_2A_5(B_5B')_2$
B4111	4	1:1	1	$B(B_5A_4A')_4$
B3211	3	2:1	1	$B'B_5(A_4A')_2$
B2411	2	4:1	1	$(A'A_4)_2B_6(A_4A')_2$
A4112	4	1:1	2	$A(A_9B_{11}B')_4$
A3122	3	1:2	2	$A'A_9(B_{11}B')_2$
A2142	2	1:4	2	$(B'B_{11})_2A_{10}(B_{11}B')_2$
B4112	4	1:1	2	$B(B_{11}A_9A')_4$
B3212	3	2:1	2	$B'B_{11}(A_9A')_2$
B2412	2	4:1	2	$(A'A_9)_2B_{12}(A_9A')_2$

\* Describes the multiple of chain length based on  $A_5$  and  $B_6$ .

Second, the interaction energies of various types of beads are defined by the Flory-Huggins interaction parameters,  $\chi$ . Multiplication by  $RT$ , where  $R$  is the molar gas constant and  $T$  is the temperature, results in the interaction parameters  $\varepsilon_{AB}$ , which is expressed in the units of  $\text{kJ} \cdot \text{mol}^{-1}$ . The  $\varepsilon_{AB}$  values in a range of ratios between A and B are listed in Table 2. A positive  $\varepsilon_{AB}$  value corresponds to a repulsion interaction between components A and B. The local gradients of the chemical potentials provide the driving force for diffusion. A set of functional Langevin equations was applied to describe the dynamics of the component densities.

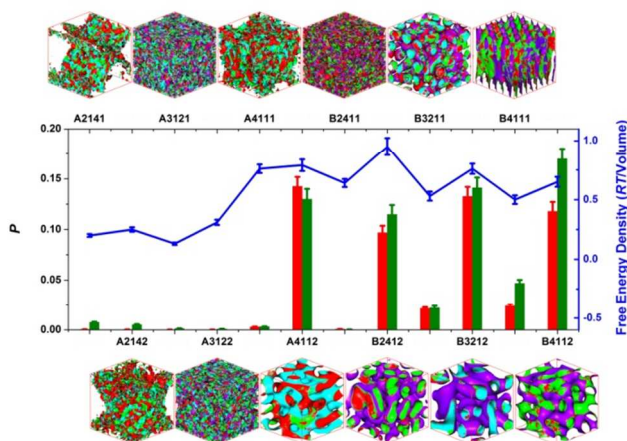


**Fig. 2**  $P$  and free energy density values of twelve PEO-*b*-PMMA BCPs. The red column is the  $P$  value of the EO beads, and the green column is the  $P$  value of the MMA beads. The phase morphologies of the short-chained BCPs are listed at the top according to the order on the upper  $X$  axis, and the bottom ones are long-chained. Here, red represents the A isosurface, purple represents the  $A'$  isosurface, green represents the B isosurface, and cyan represents the  $B'$  isosurface.

**Table 2**  $\varepsilon_{AB}$  data converted from  $\chi$  values via molecular dynamics [29] calculations at 400 K.

Ratio of A to B segment	$\varepsilon_{AB}$
1:1	3.61
1:2	1.14
1:4	0.24
2:1	4.68
4:1	6.23

Finally, except for the Flory-Huggins parameters, the phase behavior of the constructed polyelectrolytes is also governed by electrostatic interactions (i.e., the Donnan effect) [14]. It is assumed that the volume of the ions is negligible compared to that of the bead species in the system. The interactions between the charged beads are shown by  $\chi_{AB}^D$  in salt strength. In a zeroth order approximation,  $\chi_{AB}^D = \frac{\chi_{AB}}{C}$ , where  $A$  and  $B$  are the valences of beads A and B, respectively, and  $C = 2\nu C_s$  is the number of ions in the ion bath per unit of bead volume. When the salt strength is high or the electrostatics is low, the zeroth order approximation would be sufficient for most applications [14, 30-31]. Apparently, the PEO-*b*-PMMA polyelectrolyte conforms to this approximation. In addition, the salt strength of the fluid mediates the electrostatic interactions.

All of the simulations in this study were carried out in a  $32 \times 32 \times 32 \text{ nm}^3$  periodic cubic cell. The grid parameter was  $d = a \cdot h^{-1} = 1.1543$ , where  $a$  is the bond length and  $h$  is the mesh size. To ensure a stable numerical algorithm, all of the bead diffusion coefficients were set to  $1.0 \times 10^{-7} \text{ cm}^2 \cdot \text{s}^{-1}$  as an approximation. For numerical speed and stability, a constant noise-scaling parameter of 100 was chosen, and the compressibility parameter was fixed at 10.0. The total dimensionless time was 100,000 steps for each simulation (i.e., 5.0 ms) with a time step  $\Delta t = 50 \text{ ns}$  (dimensionless time step  $\Delta t = 0.5$ ) [32]. Therefore, the dimensionless time step used by the MesoDyn simulation engine was 0.5, with the definition as the production of the time step being multiplied by the bead diffusion coefficient, then divided by the square of the grid spacing. The ambient temperature was chosen to be 400 K. At this temperature, the PEO-*b*-PMMA BCPs exhibit positive  $\chi$  values in a wide range of compositions. Due to the cation or anion concentration being obtained from the salt strength through division by the cation or anion absolute valence, the salt strength was set to  $0.01 \text{ mol} \cdot \text{L}^{-1}$ . To confirm the electrostatics of A and B beads, the ab initio calculations were performed on the PEO and PMMA homopolymers, using the Gaussian 03 software with the RM062X method and 6-311++G(d, p) basis sets. By converting the Mulliken charges into the coarse-grained beads, -0.21, 0.42, -0.03 and 0.06 were distributed to A,  $A'$ , B and  $B'$ , respectively.

### 3 Results and Discussion

The phase separation dynamics can also be characterized by the time evolution of the average order parameter,  $P_i$ , which is defined as the volume average of the difference between the local density squared and the overall density squared:

$$P_i = \frac{1}{V} \int [\eta_i^2(r) - \eta_i^2] dr,$$

where  $\eta_i$  is a dimensionless density (volume fraction) for species  $i$ .  $P$  values should asymptotically approach a stable value as the system attains dynamic equilibrium. Therefore,  $P$  is a significant index of the degree of phase separation where a large value indicates strong phase segregation and a very small value indicates a mixed state. In addition, the free energy density [33-34] can be a good index for evaluating the dynamic state, and the free energy density is calculated based on dynamic mean-field density functional theory. Therefore, this density is not routinely calculated for real systems, and it is not possible to make a direct comparison with experimental free energy data [35].

### 3.1. Aggregation structures of the twelve designed BCPs

The observed phases in Fig. 2 include the disorder (A2141), disorder (A2142), disorder (A3121), disorder (A3122), disorder (A4111), bicontinuous (A4112), disorder (B2411), worm-like micelles (B2412), mixed micelles (B3211), irregular micelles (B3212), crossed lamellar (B4111) and bicontinuous (B4112) phases. The analysis is described below. Being similar to the molecular structure of B3211, the Y-shaped copolymer also self-assembled into micelles via experimental analyses [36-37], which indicates the importance of the molecular topologies in phase morphologies.

(1) In general, both the  $P$  and free energy density values of long-chained BCPs are higher than those of the corresponding short-chained ones. Due to the long chains of both the A and B segment of long-chained BCPs, more space is available for different segments to adjust their orientation to find more opportunities to assemble with the same segments. Then, the microphase formed and phase separation occurs. The results reflect the high  $P$  values. In addition, the longer chain, which has more beads, induces a higher enthalpy, and the higher  $P$  causes a loss of entropy. The synergistic effect of both the enthalpy and entropy changes for long-chained BCPs results in a higher free energy density.

(2) Both A4112 and B4112 are long and consist of the same number of A and B segments. In addition, their arm number is the highest, which provides more opportunities to assemble the same component together resulting in the formation of the bicontinuous phase. The outer components are A and B' for A4112. In contrast, when the A and B segments are exchanged, the molecular structure converts from A4112 to B4112 where the A' and B segments are outside. Therefore, the phase morphologies of A4112 and B4112 are conjugated.

(3) The molecular topologies of B3211 and B3212 mimic the basic molecular structure with one hydrophobic and two hydrophilic tails. Therefore, both of their phase morphologies are micelles. Compared with B3211, there are more beads in the long-chained B3212, making the arms of B3212 have more degree of freedom to move and adjust its orientation. Therefore, the formed aggregates are larger and more orderly than short-chained B3211, which is indicated by the higher  $P$  value. For B2412, its molecular structure resembles a combination of two B3212 BCPs joined together at the end of the hydrophobic B beads to form more symmetrical micelle

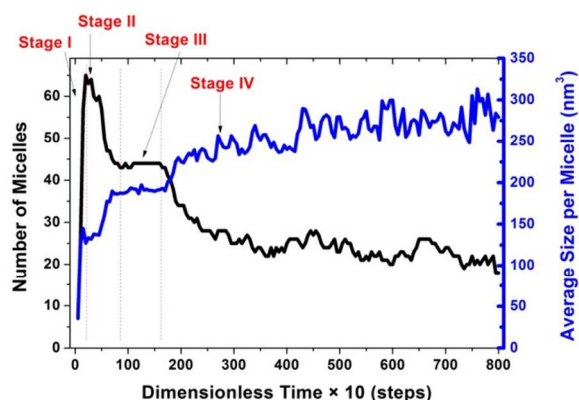


Fig. 3. Time evolution of the number of micelles and the average size per micelle of B2412.

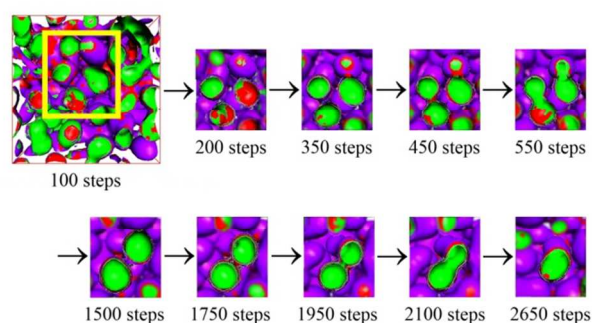


Fig. 4. Evolution of the representative phase morphology landscape of B2412. The area enclosed by the yellow box is enlarged and placed on the right to show the process in detail.

aggregates than that from the self-assembly of B3212 due to the higher symmetry of the B2412 molecule. However, B2412 formed worm-like micelles, which is different from the spherical micelles formed by unchanged B2412. This result occurs due to the introduction of the Donnan effect causing a loss of translational entropy, which is significant for phase separation leading to an increase in solubility of the charged component in the bulk of the other component. Surprisingly, the B2411 BCP, which has the same molecular topology as B2412, doesn't form an obvious micelle-like phase from its mesoscopic performance.

However, the high free density value of B2411 indicates its uniqueness. Next, 71 small aggregates with an approximate volume of  $40 \text{ nm}^3$  were dispersed in the system. The short-chained molecular structure of B2411 results in aggregates that are more compact than B2412. In addition, the short chain reduces the flexibility of the arms, which prevents the assembly from continuing. Therefore, this defect in B2411 is related to the chain length.

(4) The situation for A4111 is similar to that of B2411, and 233 small aggregates were found to exist randomly in the system with a volume approximately  $37 \text{ nm}^3$ . Therefore, due to increase in the number of aggregates, both the  $P$  and free energy density values of A4111 are slightly higher than those of B2411.

(5) All of the phase morphologies of A2141, A2142, A3121 and A3122 exhibit disorder, and no aggregates were observed in the system, which results in the lowest four free energy density values. Although their molecular topologies are conjugated with B2411, B2412, B3211 and B3212, the phase morphologies are different. The lipid-like structured A3121 and A3122 have two hydrophobic and one hydrophilic arms. However, A2141 and A2142 are a combination of A3121 and A3122 with the two terminals of the "A" segments join together. The molecular structure and high B segments, compared to the segments formed, dictate the phase morphology (A2141, A2142, A3121 and A3122) behavior being different from that of their conjugate BCPs (i.e., B2411, B2412, B3211 and B3212).

(6) Based on this discussion, a BCP with a B bead as the branching point results in an easily formed ordered phase, especially for long-chained BCPs. The B4111 is a special case with the highest  $P$  value among the short-chained BCPs. Both the upper and the lower part of the system form a lamellar phase but their orientations are perpendicular to each other, i.e., crossed lamellar.

### 3.2. Transition phase structure and mechanism of B2412 BCP

To form the micelle phase of B2412 BCP, the transition mechanism of the mesostructure is based on the changing processes related to the number of micelles and the average size per micelle, as shown in Fig. 3. In conjunction with the evolution of snapshots shown in Fig. 4, the phase formation mechanism can be compressively understood. For clarity, we extracted one portion of the system to highlight our target segments.

The theoretical concept that elongated molecules spontaneously organize into orientation ordered phases has lasted for over fifty years. At first, the physical basis of self-ordering in these theories is the minimization of repulsive forces in condensed assemblies [38-39]. Later on, Maier and Saupé attempted to incorporate anisotropic attractive forces in the theory of liquid crystallinity [40]. In an effort to include effects related to semiflexibility in self-ordering chains, various modifications of original theories have been achieved [41-44]. In Fig. 3, four stages of micellar evolution can be observed including the induction stage, fast-growth stage, adjustment stage and slow-growth stage. In Stage I, many small micelles were generated, and the number of micelles reaches a maximum at 200 steps, i.e., 65 micelles. Next, the number of micelles decreases quickly to 45 during the next 500 steps in Stage II. Therefore, small micelles grow into larger micelles, and the size per micelle increases by 48.8 %. Then, a stable stage with nearly no change in both the number of micelles and average size per micelle occurs for 1,100 steps. This stage is considered Stage III. After the adjustment stage, the micelle growth begins again, and in Stage IV, this growth rate is slower than that observed in Stage II based on the gradient of the average size per micelle as a function of time.

Based on this description, a fusion mechanism was proposed, as shown in Fig. 4. At 100 steps, many small-sized segments are randomly dispersed in the system. Four independent segments were selected as the target to elaborate the phase forming process. The components inside the bottom right segment change the orientation of the arrangement, and this micelle approaches the upper one after 100 steps during the induction stage (Stage I). At 350 steps, this micelle buds onto the upper one and requires 100 steps to open the shell of the upper micelle. Then, the upper micelle transfers its B segments into the bottom one via a narrow channel between these two micelles, and the transition morphology takes the form of a peanut with a narrow neck. The same process occurs for on the coalescent of the couple segments on the left. These segments are in the fast-growth stage (Stage II). Both of these couples adjust their shape from peanut to round, which is maintained for 950 steps during the adjustment stage (Stage III). In addition, the two newly born micelles approach each other, and both micelles first open their shells at 1,750 steps. Then, these micelles fuse the contents inside with the neck of the joint part becoming wider. 700 steps are required to adjust the final large segment into a micellar shape during the slow-growth stage (Stage IV). This fusion process depicts the integration of four

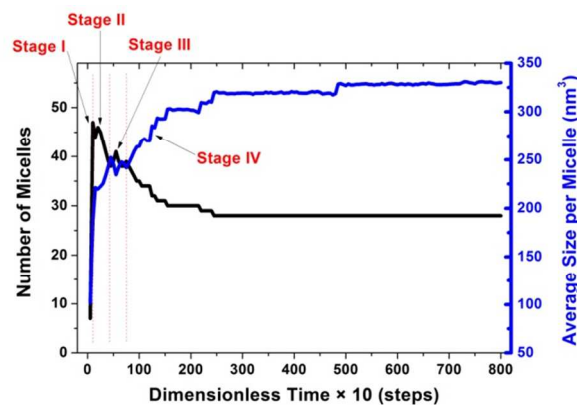


Fig. 5. Time evolution of the number of micelles and the average size per micelle of B2412.

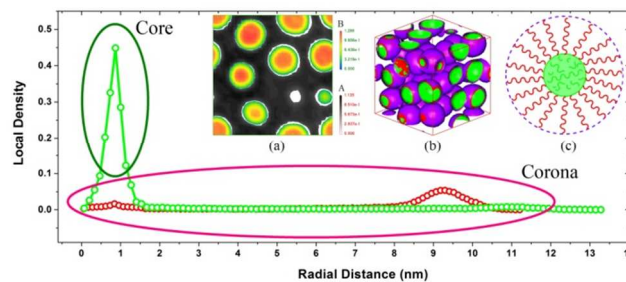


Fig. 6. Indicated density profiles of the A and B beads as a function of the radial distance from the micelle core. (a) Density slice of both the A and B beads. (b) Snapshot of mesoscale structure. (c) Schematic structure of the spheroidal micellar phase.

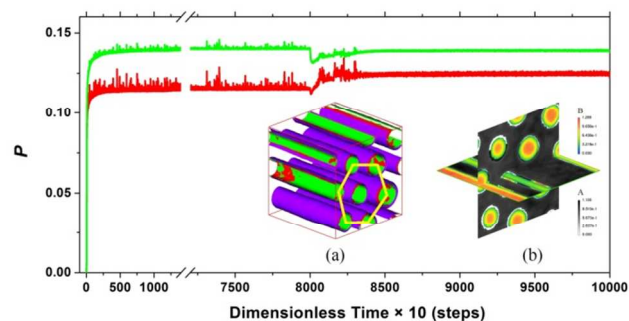
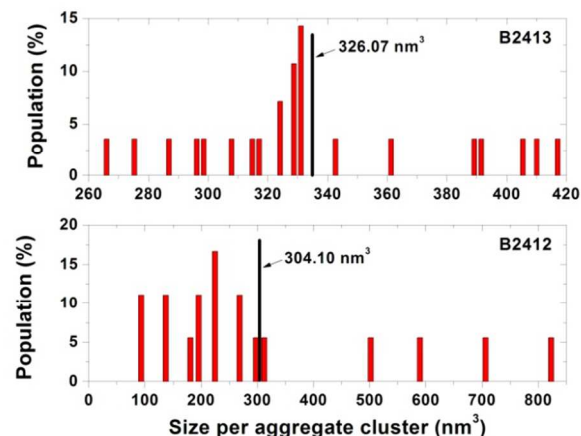


Fig. 7. Time evolution of the  $P$  values. (a) Snapshot of mesoscale structure subjected to the shear effect. (b) The density slice of both the A and B beads vertical to and along the direction of shear stress.



**Fig. 8.** Population of B2412 and B2413 as a function of the size per aggregate cluster.

small micelles into two larger micelles followed by the combination of the two larger ones into a single large micelle.

5 These results are consistent with a decrease in the number of micelles and an increase in the average size per micelle. All four stages have been illustrated.

### 3.3. Analysis of the phase morphology of B2413 BCP

To investigate the phase morphology of BCP with different chain lengths, we doubled the length of the A and B segments based on B2411 to generate B2413 BCP. The phase forming process of B2413 was studied using the same method used for B2412 via the analysis of the number of micelles and the average size per micelle in Fig. 5. Four stages were observed during the fusion process, and the only difference compared to B2412 was the residence time, i.e., 300 steps, which is approximately 30 % of the residence time for B2412 (i.e., 950 steps). Due to its longer arm structure, which is more flexible than the short-chained B2412, B2413 requires less time to adjust its arrangement. In addition, the time required to reach a dynamic equilibrium state is only 2,500 steps. In comparison to B2412, the number of micelles and average size per micelle are both larger at the equilibrium state, and the formation of micelles requires less time and occurs much faster.

25 As shown in Fig. 6, two unimodal and narrow peaks were observed for the density distributions, which indicates that the hydrophobic MMA blocks aggregate to form the very high density core structure of the micelle and the hydrophilic EO blocks constitute the corona structure. The density field distributions were mapped into two-dimensional pictures, as shown in Fig. 6a. A micellar phase consists of a dense core composed of B beads and a dense corona composed of A beads. In addition, the stable structure shown in Fig. 6b indicates that the outer portion of the corona is only the terminal of the A segments. Therefore, the core-shell structure of the spherical micellar structure is shown in Fig. 6c.

In Fig. 7, a homogeneous phase is a start, and in a short time, many small micelles are generated, which is accompanied by a rapid increase of the  $P$  value. After the coalescent of small micelles into large ones by the fusion mechanism discussed above, the system maintains dynamic equilibrium for approximately 78,000 steps. A steady shear,  $\gamma$ , was set to  $5 \times 10^5 \text{ s}^{-1}$ , which was exerted after 80,000 steps to reflect the stirring condition. This disturbance breaks the previously ordered system, and quasi-spherical micelles are dragged and transformed into a columnar morphology along the direction of shear. After the formation of columnar micelles, the  $P$  value increases quickly. The subsequent  $P$  values are very stable, reflecting less fluctuation. This result indicates that the system has no defects once the columnar micelles are formed. Notably, the columnar micelles convert to an ordered hexagonal arrangement, as shown in Fig. 7a. Two density slices originate from the phase morphology shown in Fig. 7a where one slice is vertical to the shear rate and the other is along the direction of shear rate. Such an orthogonal density slice of the A and B beads is indicative of the core-shell columnar structure. In this structure, the B beads form the dense core, the A beads constitute the corona and the

terminal of the A segments is

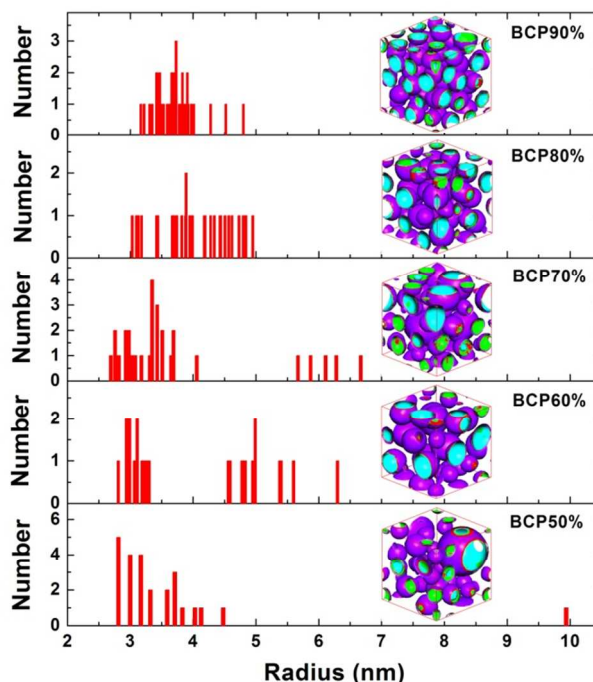


**Fig. 9.** Numerical statistics for the radius of micelles for the blending systems with B2412 concentrations of 50 %, 60 %, 70 %, 80 % and 90 %. The corresponding mesoscale structures are also shown.

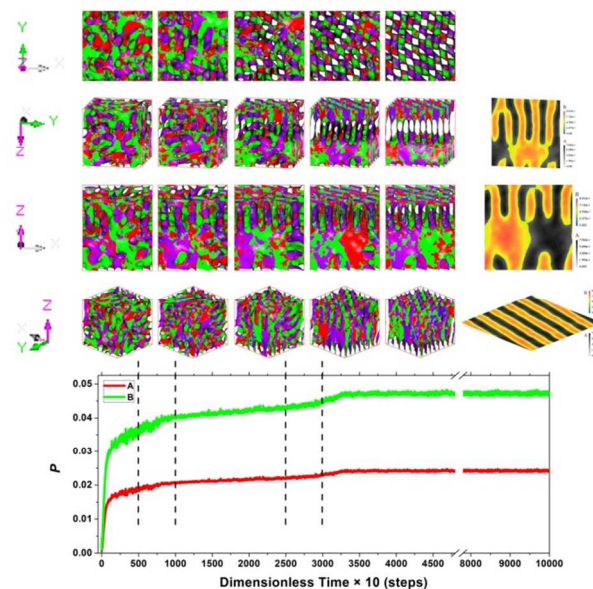


**Fig. 10.**  $P$  values of B4111 as a function of the evolution of time. The representative phase morphologies for each stage are shown in the specified perspectives as denoted in the axis in each line. Three density slices of the YZ, XZ and XY planes are shown from top to bottom, corresponding to the phase morphologies on the left.

the outer of columns, which maintains the same micelle composition in two dimensions.

### 3.4. Comparison between B2412 and B2413

Although both the B2412 and B2413 system form micellar phases, their micelle distributions are quite different, as shown in

Fig. 8. The chain length of B2413 is 0.5 times larger than that of B2412, according to the scaling factor of  $R_g$  (the radius of gyration) of a polymer being proportional to  $N^{1/3}$  ( $N$  is the number of particles on a chain) in poor solvent, so theoretically, the equivalent size of micelle for B2413 should be 0.5 times larger than that B2412. However, as calculated, the average size per micelle of B2413 ( $326.07 \text{ nm}^3$ ) were calculated to be only 0.072 times larger than that of B2412 ( $304.10 \text{ nm}^3$ ). This result is due to the long-chained BCP being more flexible with freedom to adjust their orientation. Then, the arms adopt coil-like conformations in both the core and corona areas.

It is necessary to define a new index,  $PDS$ , to specify the polydispersity of different micelles sizes.  $PDS$  is equal to the average size per micelle divided by the arithmetic mean value of the range of sizes. Therefore, a small  $PDS$  value indicates micelles with a uniform size. In contrast, a large  $PDS$  value indicates micelles with many different sizes, and the range of sizes is wide. The  $PDS$  value of B2413 was 1.05, which is smaller than that for B2412 (1.51). This result indicates the micelle sizes are more uniform for B2413, which is consistent with their phase morphologies. The molecular structure of BCP, which consists of long-chained BCP with long arms, possess more freedom of movement and more opportunities to assemble with the same segments to form large aggregates.

A system with well-distributed micelles is stable in applications. However, when there are multistep-distributed micelles dispersed in a system, the performance would be step by step or even unstable. A trial simulation of the A10/B12 homopolymer blends, which are the components of B2412, was performed. The equilibrium mesoscopic structure contains six small spherical micelles with a volume of  $43.4 \text{ nm}^3$  and one large spherical micelle with a volume of  $6583.6 \text{ nm}^3$ . Therefore, the blends with B2412, A10 and B12 can regulate the size distribution. In Fig. 9, the mesoscale structures at various B2412 concentrations are present as a spherical micellar phase. Therefore, we utilized the radius to characterize the polydispersity ( $PDR$ ), and the definition is similar to that of  $PDS$ . The average radii of the micelles in the systems with B2412 concentration of 50 % to 90 % are 3.60 nm, 4.09 nm, 3.73 nm, 4.04 nm and 3.65 nm, and the  $PDR$ s are 0.99, 0.43, 0.53, 0.24 and 0.22. The blending of the constituents is a good technique to amend the shape of micelles from elliptical to irregular and spherical, which is consistent with our expectation. In particular, a small amount of homopolymer doping (B2412 90 %) can efficiently improve the uniformity of the micelle size. Such mutual compensation for regulating the size of both BCP and homopolymers produces a lower polydispersity in their mixed systems, which is primarily dependent on the homopolymers. In comparison to BCP, the volume and size of the homopolymers are both smaller, which is beneficial to the diffusion in the system, and the diffusion velocity is high, which results in easier size compensation. In contrast, for the system with a large quantity of homopolymers, this compensation effect stabilizes the size of micelles, due to the assembly of only homopolymers.

### 3.5. New Phase Morphology of B4111

Based on the  $P$  values as a function of time shown in Fig. 10, 32,000 steps are required to achieve dynamic equilibrium, which is much longer than that of other BCPs. In the beginning, many

curved small planes were formed. However, small holes were generated in the planes, and a fast increase in the  $P$  values was observed. During the 5,000 steps period, the small holes move and fuse into medium holes in a random distribution, and the acceleration in the  $P$  values decreases, due to the movement of the holes. In the time-consuming process of sequentially adjusting the holes, which require 20,000 steps, the increasing rate of the  $P$  values increases slightly. After 2,600 steps, the vertical holes fine tune their orientation resulting in the formation of a slightly distorted lamellar phase. Interestingly, the phase formation process described above occurs simultaneously, where two sets of lamellar phases are generated in both the upper half and the lower half parts with the respective density slices in the YZ and XZ plane. This new phase is called the crossed lamellar phase. This new phase is due to the unique molecular topology of B4111 and its short chain length. The short-chained structure provides a flexible orientation and fast diffusion, which facilitate its translational motion (the movement of the holes) and rotation (the reorientation of the holes). The characteristics of the molecular topology of B4111 include (1) four arms with different components joined at one B bead, which leaves a large vacant area between the adjacent arms that can be occupied by other components. In addition, (2) the outer portion of this molecule composed of only A segments, which provides more opportunity for the same components to assemble together, and (3) the rotation of the two opposite arms around the axis of the other two opposite arms is optional and free, which results in the generation of the crossed two lamellar phases.

## 4 Conclusions

The self-assembly of weak polyelectrolyte PEO-*b*-PMMA BCPs were investigated with the aid of MesoDyn simulations. The twelve models designed with various molecular topologies and different chain lengths were studied. The typical phase morphologies include disorder (A2141, A2142, A3121, A3122, A4111 and B2411), bicontinuous (A4112 and B4112), worm-like micelles (B2412), mixed micelles (B3211) and irregular micelles (B3212). A new type of morphology, i.e., crossed lamellar phase, was generated by B4111.

We concentrated on B2412, due to its micellar phase. The number of micelles and the average size per micelle as a function of time were analyzed, and four stages were observed including the induction stage (Stage I), fast-growth stage (Stage II), adjustment stage (Stage III) and slow-growth stage (Stage IV). In combination with the evolution of the representative phase morphologies, a fusion mechanism was proposed for the formation of the phase morphology of B2412. When the chain length was 0.5 times longer than that of B2412, B2413 was generated, which produced a spherical micelle phase with a uniform size distribution. The density slice indicates a core-shell structure. Herein, the MMA blocks constitute the dense core and EO forms the corona. After application of a moderate shear force, a perfect hexagonal columnar phase was generated, and the same core-shell structure was maintained. We also explored blending B2412 and homopolymers with different BCP concentrations to regulate the uniformity of the micelle size and polydispersity. The blends with a small amount of homopolymer have the most uniform distribution of micelle size. In addition, the

polydispersity was low.

A unique type of mesoscopic structure, crossed lamellar phase morphology, was generated by B4111. Based on a dynamic perspective, we have explained the phase formation mechanism, which provides insight into designing new types of materials.

## Acknowledgments

This work is supported by the National Natural Science Foundation of China (21203164).

## Notes and references

<sup>a</sup> Institute of Research on the Structure and Property of Matter, Zaozhuang University, Zaozhuang, 277160, China. E-mail: mudanjlu1980@163.com.

<sup>b</sup> Opto-Electronic Engineering College, Zaozhuang University, Shandong 277160, China. E-mail: lij786@163.com.

<sup>c</sup> School of Chemistry and Chemical Engineering, Shandong University, Jinan, 250100, China; E-mail: fsy@sdu.edu.cn.

- 1 Y. Mai and A. Eisenberg, *Chem. Soc. Rev.*, 2012, **41**, 5969.
- 2 A.Z. Samuel and S. Ramakrishnan, *Macromolecules*, 2012, **45**, 2348.
- 3 S. Mann, *Nat. Mater.*, 2009, **8**, 781.
- 4 J. Dhar and S. Patil, *ACS Appl. Mater. Interfaces*, 2012, **4**, 1803.
- 5 S. Peleshanko, V.V. Tsukruk, *J. Polym. Sci. Part B: Polym. Phys.*, 2012, **50**, 83.
- 6 S. Chen, S.X. Cheng and R.X. Zhuo, *Macromol. Biosci.*, 2011, **11**, 576.
- 7 L.H. Sperling, *Introduction to Physical Polymer Science*, John Wiley & Sons, Hoboken, New Jersey, 2006.
- 8 H. Tanaka, *Phys. Rev. Lett.*, 1996, **76**, 787.
- 9 H. Tanaka, *Phys. Rev. Lett.*, 1993, **71**, 3158.
- 10 H. Tanaka and T. Araki, *Chem. Eng. Sci.*, 2006, **61**, 2108.
- 11 M. Rubinstein and R. H. Colby, *Polymer Physics*, Oxford University Press: Oxford, UK, 2003.
- 12 S. Thomas, D. Durand, C. Chassenieux and P. Jyotishkumar, *Handbook of Biopolymer-Based Materials: From Blends and Composites to Gels and Complex Networks*, John Wiley & Sons, 2013.
- 13 F. Oosawa, *Polyelectrolytes*, Marcel Dekker, New York, 1971.
- 14 A.V. Kyrlyuk and J.G.E.M. Fraaije, *J. Chem. Phys.*, 2004, **121**, 2806.
- 15 N.S. Cameron, A. Eisenberg and G.R. Brown, *Biomacromolecules*, 2002, **3**, 124.
- 16 S. Förster, N. Hermsdorf, W. Leube, H. Schnablegger, M. Regenbrecht, S. Akari, P. Lindman and C. Böttcher, *J. Phys. Chem. B*, 1999, **103**, 6657.
- 17 M. Regenbrecht, S. Akari, S. Förster and H. Möhwald, *J. Phys. Chem. B*, 1999, **103**, 6669.
- 18 J.L. Barrat and J.F. Joanny, *Adv. Chem. Phys.*, 1996, **XCIV**.
- 19 C. Holm, J.F. Joanny, K. Kremer, R.R. Netz, P. Reineker, C. Seidel, T.A. Vilgis and R.G. Winkler, *Adv. Polym. Sci.*, 2004, **166**, 67.
- 20 S. Förster and M. Schmidt, *Physical Properties of Polymers*, Springer, 1995.
- 21 V.Y. Borue and I.Y. Erukhimovich, *Macromolecules*, 1988, **21**, 3240.
- 22 A.N. Kudlay, I.Y. Erukhimovich and A.R. Khokhlov, *Macromolecules*, 2000, **33(15)**, 5644.
- 23 M. Castelnovo and J.F. Joanny, *Macromolecules*, 2002, **35(11)**, 4531.
- 24 A.V. Dobrynin, *Macromolecules*, 2006, **39**, 9519.
- 25 N.P. Shusharina, E.B. Zhulina, A.V. Dobrynin and M. Rubinstein, *Macromolecules*, 2005, **38(21)**, 8870.
- 26 Q. Liao, A.V. Dobrynin and M. Rubinstein, *Macromolecules*, 2006, **39**, 1920.
- 27 J.G.E.M. Fraaije, B.A.C. van Vlimmeren, N.M. Maurits, M. Postma, O.A. Evers, C. Hoffmann, P. Altevogt and G. Goldbeck-Wook, *J. Chem. Phys.*, 1997, **106**, 4260.
- 28 B.A.C. van Vlimmeren, N.M. Maurits, A.V. Zvelindovsky, G.J.A. Sevink and J.G.E.M. Fraaije, *Macromolecules*, 1999, **32**, 646.
- 29 D. Mu, X.R. Huang, Z.Y. Lu and C. C. Sun, *Chem. Phys.*, 2008, **348**, 122.
- 30 S.L. Yuan, X.Q. Zhang, G.Y. Xu and D.J. Zhang, *J. Mol. Model.*, 2006, **12**, 406.
- 31 A.V. Kyrlyuk and J.G.E.M. Fraaije, *J. Chem. Phys.*, 2004, **121(18)**, 9166.
- 32 S.R. de Groot and P. Mazur, *Non-Equilibrium Thermodynamics*, Dover Publications: New York, 1983.
- 33 J. Fraaije, B. Van Vlimmeren, N. Maurits, M. Postma, O. Evers, C. Hoffmann, P. Altevogt and G. Goldbeck-Wood, *J. Chem. Phys.*, 1997, **106**, 4260.
- 34 P. Altevogt, O.A. Evers, J.G.E.M. Fraaije, N.M. Maurits and B.A.C. van Vlimmeren, *J. Mol. Struct-Theochem.*, 1999, **463**, 139.
- 35 S.S. Jawalkar and T.M. Aminabhavi, *Polymer*, 2006, **47(23)**, 8061.
- 36 Y.F. Chu, H. Yu, Y.T. Zhang, G.Y. Zhang, Y.Y. Ma, R.X. Zhuo and X.L. Jiang, *J. Polym. Sci., Part A: Poly. Chem.*, 2014, **52**, 3346.
- 37 K. Skrabanja, A. Laschewsky, H.V. Berlepsch and C. Böttcher, *Langmuir*, 2009, **25(13)**, 7594.
- 38 A. Onuki and K. Kawasaki, *Dynamics and Patterns in Complex Fluids*, Springer, Heidelberg, 1989.
- 39 K. Kawasaki, M. Tokuyama and T. Kawakatsu, *Slow Dynamics in Condensed Matter*, American Institute of Physics, New York, 1992.
- 40 P.G. de Gennes, *Scaling Concepts in Polymer Physics*, Cornell University, Ithaca, 1979.
- 41 T. Kawakatsu and K. Kawasaki, *Physica A*, 1990, **167**, 690.
- 42 T. Kawakatsu and K. Kawasaki, *Molecular Dynamics Simulations*, Springer, Berlin, 1992.
- 43 T. Kawakatsu and K. Kawasaki, *J. Colloid Interface Sci.*, 1991, **145**, 413.
- 44 T. Kawakatsu and K. Kawasaki, *J. Colloid Interface Sci.*, 1991, **148**, 23.